

# Engineering inter-band coupling in a two-band superconductor by topological defects

Thomas Gozliniski,<sup>1,\*</sup> Qili Li,<sup>1,†</sup> Rolf Heid,<sup>2</sup> Oleg Kurnosikov,<sup>3</sup> Alexander Haas,<sup>1</sup>  
Ryohei Nemoto,<sup>4</sup> Toyo Kazu Yamada,<sup>4,5</sup> Jörg Schmalian,<sup>6,7</sup> and Wulf Wulfhekel<sup>1,6</sup>

<sup>1</sup>*Physikalisches Institut, Karlsruhe Institute of Technology, 76131 Karlsruhe, Germany*

<sup>2</sup>*Institute for Quantum Materials and Technologies,  
Karlsruhe Institute of Technology, 76131 Karlsruhe, Germany*

<sup>3</sup>*Universite de Lorraine, Institute Jean Lamour, France*

<sup>4</sup>*Department of Materials Science, Chiba University,  
1-33 Yayoi-cho, Inage-ku, Chiba 263-8522, Japan*

<sup>5</sup>*Molecular Chirality Research Centre, Chiba University,  
1-33 Yayoi-cho, Inage-ku, Chiba 263-8522, Japan*

<sup>6</sup>*Institute for Quantum Materials and Technologies,  
Karlsruhe Institute of Technology, 76344 Eggenstein-Leopoldshafen, Germany*

<sup>7</sup>*Institut für Theorie der Kondensierten Materie,  
Karlsruhe Institute of Technology, 76131 Karlsruhe, Germany*

(Dated: May 13, 2025)

# Abstract

The vast majority of superconductors have more than one Fermi surface, on which the electrons pair below the critical temperature  $T_C$ , yet their superconducting behavior can be well described by a single-band Bardeen-Cooper-Schrieffer theory. This is mostly due to inter-band scattering, especially in superconductors in the dirty limit, rigidly linking the pairing amplitude of the different bands. This effect has severely limited experimental studies of the complex physics of multi-band superconductivity. In this study, we utilize the fact that elementary Pb - as a clean limit system - has two Fermi surfaces that are only weakly coupled by inter-band scattering, allowing the formation of two separate condensates. By studying elementary crystal defects in the form of stacking faults with our millikelvin scanning tunneling microscope, we show how to locally tune inter-band coupling ranging from weak to strong coupling and modify the superconducting order parameters around defects. The experiments critically test the theory of multi-band superconductors and give a route to access a wide range of predicted quantum effects in these systems.

## I. INTRODUCTION

Microscopic attractive interactions between electrons that lead to conventional superconductivity are captured by the Bardeen-Cooper-Schrieffer (BCS) theory [1] in an elegant and transparent form. BCS theory successfully predicts the temperature dependence of the superconducting gap or the shape of the quasiparticle spectrum, as measured in a tunneling experiment. In some sense, the theory performs even better than expected. Although, in its most elementary form, it only considers a single electronic band and a perfectly clean environment, it can still describe the tunneling spectra measured on many real superconducting materials. As an extension, the finite effective quasiparticle lifetimes, e.g. due to scattering by non-magnetic crystal imperfections or inelastic scattering processes were also considered by Dynes and others [2, 3]. Most superconductors in nature have more than one electronic band crossing the Fermi energy, which should allow electrons to scatter between different bands in the normal state and, in principle, also lead to superconductivity in multiple bands. Multiband superconductivity was first suggested by Suhl, Matthias and Walker

---

\* These authors contributed equally to this work.

† These authors contributed equally to this work.; Corresponding author: qili.li@kit.edu

(SMW) [4], only two years after the seminal theory by BCS, and highlighted the case of two non-interacting bands. Without inter-band pairing interaction, the individual bands are expected to develop distinct superconducting gaps that emerge at distinct transition temperatures ( $T_c$ ) [4]. The reason behind the single-band BCS theory's long success lies in the fact that scattering between multiple bands couples these distinct pairing amplitudes which now emerge at a single  $T_c$ . In the limit of strong coupling between bands of similar density of states at the Fermi level, the gap values merge to a common value due to an inter-band proximity effect [5, 6] in momentum space [7, 8]. This process can be due to inter-band electron-phonon or electron-electron interactions in clean systems. It becomes unavoidable in 'dirty' superconductors or at temperatures close to  $T_c$ , where electron lifetimes become shorter. This leads to the appearance of a single pairing condensate with essentially a single lifetime-broadened superconducting gap [4, 7, 9, 10], that disguises the multiband nature of the material. According to Anderson's theorem, the gap and the transition temperature are robust against nonmagnetic scatterings for single-band conventional superconductors [11]. However, in full agreement with our above statements, generalizations to multi-band superconductors show that nonmagnetic scattering changes the superconducting gap values as long as their magnitudes are distinct [12]. Robustness against nonmagnetic impurities reemerges once a common gap value has been established.

With advancements in the growth of high-quality superconductor crystals and improvements in low-temperature measurement techniques, it has become possible to discern the energy differences among individual superconducting gaps in several clean multiband systems [13–18]. Among these materials, bulk lead (Pb) stands out as an elemental two-band superconductor [17, 19–21] that is available in exceptional purity and crystallinity. Pb displays two Fermi surfaces, a compact one and an open one (see e.g. [22] and Fig. 1(d) and (c)). Recent experimental results further indicate that the inter-band coupling in Pb is rather weak [21], such that at low temperatures, two superconducting gaps in the tunneling spectrum appear. The compact Fermi surface of Pb gives rise to the larger gap ( $\Delta_2$ ) and the open Fermi surface to the smaller one ( $\Delta_1$ ) [20, 21]. This makes Pb an ideal model system for experimentally studying how two bands and their condensates interact, e.g. by studying how individual crystal defects alter the scattering within and between bands and change the pairing state. This allows direct insight into the microscopic scattering events that eventually limit many superconducting devices through the critical current and critical

field [23–26]. Gaining control over the inter-band coupling and scattering processes in a two-band superconductor may even give access to a wide range of predicted quantum effects, such as solitons [27, 28], vortices with fractional flux [29], non-Abrikosov vortices [30], topological knots [30], or the Leggett mode that describes excitations of the relative phase of weakly coupled bands [31].

## II. RESULTS

### A. Local superconducting density of states

A Pb(111) single crystal was cleaned by several cycles of sputtering and annealing, resulting in a surface with monoatomic steps. It was then placed on our precooling station at  $\sim 78$  K, where it was rapidly cooled before insertion into the scanning tunneling microscopy (STM) head. As a result of this procedure, few defects, which are typically challenging to prevent in the material, persist near the surface. In the constant-current STM topography Fig. 1(a), we can see three types of defects [32]: (i) small 3-5 nm sized depressions of hexagonal shape that are well known and correspond to argon bubbles or small vacancy conglomerates near the surface [33–35]; (ii) a screw dislocation, of which both ends exit the surface, leading to seemingly disrupted step edges and continuous connection of neighboring atomic terraces [36–38]; (iii) a buried stacking fault tetrahedron (SFT) of about 70 nm lateral width, which binds the screw dislocation [36] and is responsible for the weak interference pattern visible in Fig. 1(a). The SFT is an elementary crystal defect in fcc metals of low stacking fault energy [36, 39–50]. Like the smaller defects (i), it evolves from an agglomeration of vacancies that is too large in size to be energetically favoured [44, 51, 52]. Following topological rules on dislocation interactions, tensile stress is released in a process in which atoms rearrange and form a tetrahedral nanocrystal inside the bulk terminated by stacking faults [39]. Its edges feature frustrated stair-rod dislocations and each face is oriented in a (111) direction of the crystal with an intrinsic stacking fault [53, 54]. Two common ways to reliably induce SFTs in a metal are quenching [39] and ion irradiation [44]. As we find a higher density of SFTs for rapid cooling than without, we argue that both argon ion sputtering and the quick cooldown are responsible for their formation in our case. Please see Supplementary Material Note I for an SFT on the surface. A characteristic of SFTs near

the surface are quantum well states (QWS) [55, 56] that form between its triangular top (111) plane and the (111) sample surface (see Supplementary Material Note II). It is well established that these QWS allow to image sub-surface defects, including SFTs, with STM and to determine their depths below the surface [33, 34, 47, 50, 57–60]. A sketch of the measurement principle is shown in Fig. 1(b).

Beyond the modulation of the local DOS (LDOS) due to the QWS on an energy scale of hundreds of meV, the defects also locally influence superconductivity of the sample. Differential conductance ( $dI/dU$ ) maps at temperature  $T = 43$  mK [61] and at bias voltages of the bulk coherence peaks of the two superconducting gaps  $\Delta_1^0$  ( $U = 1.25$  mV) and  $\Delta_2^0$  ( $U = 1.40$  mV) [17, 21, 62] reveal SFTs through remarkable features in the LDOS on energy scales related to the superconducting gaps (see Supplementary Material Note III for determination of the intrinsic gaps  $\Delta_1^0$  and  $\Delta_2^0$  of bulk crystal). As can be seen in Fig. 1(c,d), they feature a hexagonal region of decreased LDOS at  $\Delta_1^0$  (c) and increased LDOS at  $\Delta_2^0$  (d). We point out that screw dislocations have no influence on the superconducting states in Pb(111) (see Supplementary Material Note IV). The SFT top plane appears as a triangular (or sometimes scalene hexagonal) cutout within the hexagon with slightly higher/lower LDOS in (c)/(d) and a visible in-plane quasiparticle interference pattern (see Supplementary Material Note V quasiparticle interferences by SFTs). The rod-like contours of the LDOS can be seen along the sides of the inner triangle and along the  $[10\bar{1}]$ ,  $[01\bar{1}]$  and  $[\bar{1}10]$  directions inside the outer hexagon and may be related to the stair-rod dislocations of the SFT (Supplementary Material Note I). These features in  $dI/dU$ -maps for energies at the corresponding coherence peaks of Pb [17, 19–21, 62] indicate either a local change in the spectral gap  $\Delta$  or in the intensity of the coherence peak. Owing to our low electronic temperature, we can clearly resolve the two coherence peaks at 1.25 mV and 1.40 mV in high-resolution bias spectroscopy. The top panel of Fig. 1(e) shows such a spectrum recorded far away from any SFT [21]. Taking spectra along the red line indicated in (c) confirms that the contrast in the  $dI/dU$ -maps in (c,d) stems from changes in the quasiparticle spectrum of the superconductor, i.e. the intensity of the coherence peaks and their energy (Fig. 1(e)). In the triangle region, the coherence peak of the smaller gap is very pronounced, while the coherence peak of the larger gap is suppressed. In the hexagonal region, the behavior is the opposite. In the outside region, the spectra gradually tend to the defect-free tunneling spectra on Pb(111).

In a two-band superconductor, the observed behavior can be either due to changes in

the STM tunneling matrix element or a local change in the pairing condensate. Let us first comment why we believe that the former is not at play: The momentum dependence of the tunneling matrix element between the sample and the tip leads to a variation of the tunneling spectra when varying the crystal orientation [15, 17, 63]. We argue that this effect is absent in our case, as the probed surface is of (111) orientation throughout the sample. Moreover, we studied more than 20 SFTs that all showed a common behavior namely [Fig. 2(d)-(f)]: 1. a higher coherence peak at  $\Delta_2^0$  than at  $\Delta_1^0$  in the hexagonal region irrespective of the depth and size of SFTs, 2. variations in both coherence peak intensity and energy in the triangular area for different SFTs. In the two distinct regions (triangle, hexagon) we see a variation in coherence peak energies, i.e.  $1 - (\Delta_2 - \Delta_1)/(\Delta_2^0 - \Delta_1^0)$  up to 13% for SFT#2 [Fig. 2(e)] and almost merged coherence peaks for SFT#3 [Fig. 2(f)] that cannot be explained by band sensitivity of tunneling, alone. The complete disappearance of the outer coherence peak inside the triangle (see SFT#1 in Fig. 2(d)) also speaks against the former scenario. This lends credence to the other possibility, a variation in the coherence peak energies because of a local change in the two-band superconducting condensate. This scenario allows for both, intensity changes and energy variations in the coherence peaks.

## B. Influence of scattering on the two order parameters

To understand our experimental tunneling spectra of the two-band superconductor Pb(111), we performed simulations of the density of states of an impurity-coupled two-band superconductor, following Ref. [7]. McMillan developed a model for superconductor-normal-metal sandwiches describing the proximity effect in the normal metal by scattering between the superconductor and normal metal bands [5]. Sung and Wong developed a model (S&W model) describing a mutual proximity effect in a two-band superconductor induced by inter-band scattering at non-magnetic impurities [7] which also includes intra-band scattering. Both models result in coupled equations of the two order parameters. Finally, Schopohl and Scharnberg used the S&W model in a particular form to model the DOS of two-band superconductors [8]. This model was shown to describe the tunneling spectra for MgB<sub>2</sub> [64–68], NbSe<sub>2</sub> [15, 69, 70], Ba<sub>8</sub>Si<sub>46</sub> [71], and RuB<sub>2</sub> [72]. It incorporates coupling between individual bands by allowing elastic inter-band scattering events with rates  $\Gamma_{ij}$ . This leads to a mutual proximity effect in  $k$ -space that couples the two condensates. As a consequence,

the individual gap functions  $\Delta_1$  and  $\Delta_2$  become complex and energy-dependent. For generality, here we opt for the more general Sung and Wong model- also accounting for intra-band scattering with rates  $\Gamma_i$ , as given in the Method section (see Supplementary Material Note VI for validity of the S&W model and Supplementary Material Note VII for influence of intra-band couplings).

To illustrate the effects of inter-band coupling for Pb, we show model DOS calculations in Figure 2 (a)-(c) with varying inter-band scattering, where the intrinsic gaps ( $\Delta_1^0 = 1.252$  meV and  $\Delta_2^0 = 1.40$  meV) and effective temperature ( $T = 139$  mK) were obtained from defect-free areas by fitting using the self-consistent equations in the S&W model (see Methods for details and Supplementary Material Note III). The three panels display the self-consistently calculated normalized single particle DOS with different inter-band couplings. We show results for two different values of the ratio  $\eta$  of the DOSs of the two bands:  $\eta = 0.2$  and  $\eta = 1.5$ . Naturally, for larger  $\eta$  the higher energy coherence peak is more pronounced. In the case of no inter-band coupling  $\Gamma_{21} = 0$ , the two gaps are fully decoupled and the total spectrum is just the sum of two BCS gap functions [Fig. 2(a)]. With increasing  $\Gamma_{21}$ , the two gaps begin to merge [Fig. 2(b)] and eventually become indistinguishable [Fig. 2(c)].

With the above illustration, we are able to explain our experimental tunneling spectra for different SFTs. The spectra of three representative SFTs are shown in Fig. 2(d)-(f). In the hexagonal region, c.f. purple curves in Fig. 2(d)-(f), an intermediate coupling brings the two gaps closer. In addition, the large DOS ratio  $\eta$  makes the coherence peak intensity of  $\Delta_2$  higher than that of  $\Delta_1$ . However, in the triangular region, the inter-band coupling and DOS ratio  $\eta$  vary from weak (green curve in Fig. 2(d)) to strong (red curve in Fig. 2(f)). This is due to the QWS confined above the SFT that lead to a pronounced scattering and a modulation in DOS of the compact Fermi surface, which can vary from a minimum to maximum depending on the depth of SFT (see Supplementary Material Note II for the minimum of LDOS at Fermi energy for SFT#2). For the weak inter-band coupling and very low DOS ratio  $\eta$ , only an unshifted  $\Delta_1$  is observed (green curve in Fig. 2(d)). For the medium inter-band coupling and medium DOS ratio  $\eta$ , two gaps move towards each with comparable coherence peak intensity (magenta curve in Fig. 2(e)). Eventually, for the strong inter-band coupling, the gaps have merged completely shown as red curve in Fig. 2(f). We point out that the intra-band scatterings play a role in broadening the coherence peaks (see Supplementary Material Note VII for influence of intra-band couplings). The dashed

lines mark the coherence peaks for defect-free spectra in Fig. 1(e).

### C. Spatially resolved intra- and inter-band couplings

As demonstrated in the previous section, both QWS, i.e. intra-band scattering, and inter-band couplings have a pronounced influence on the superconducting gaps. After discussing the general behavior in the two distinct regions (triangle and hexagon), we focus on the spatial dependence of intra- and inter-band scattering.

As STM allows fully spatial resolution, we mapped both intra- and inter-band coupling near defects. Figure 3 shows  $dI/dU$ -maps on a smaller SFT with an edge length of  $\sim 20$  nm. Here, the triangle region appears as a depression in the LDOS at both energies of the bulk coherence peaks,  $\Delta_1^0$  [Fig. 3(a)] and  $\Delta_2^0$  [Fig. 3(b)], due to a minimum in the normal DOS at the Fermi energy  $E_F$  [Fig. 3(c)] caused by the QWSs forming between this SFT and the surface (see also Fig. S2). Note that the  $dI/dU$ -map in Fig. 3(c) was recorded at the Fermi energy in the normal state by applying a vertical magnetic field of 300 mT. We can clearly see that the decreased/increased  $dI/dU$  signal in hexagonal region in the superconducting state shown in panel (a)/(b) is absent in the normal conducting state (c). This again highlights that the observed features are related to the two condensates and not to simple variations of the normal state DOS. We point out that the quasiparticle interference in the triangle region does not change with magnetic field, which originates from the nesting of two Fermi surfaces (Supplementary Material Note V).

On the SFT shown in Fig. 3, we recorded  $dI/dU$  spectra in a finely spaced grid and fitted them to the S&W model DOS to obtain locally resolved information on the inter- and intra-band scattering rates for each point and visualize them in a 2D map around the SFT. The results are presented in Fig. 4 (see Supplementary Material Note VIII for fitted  $\sigma_i$ ). We can see that the defect locally induced both intra- and inter-band scattering. Intra-band scattering on the open Fermi surface ( $\Gamma_1$ ) is enhanced in the hexagonal and the triangular region, while  $\Gamma_2$  is only enhanced in the hexagonal region. Most importantly, inter-band scattering is enhanced in both the hexagonal in triangular regions. Intra-band scattering is responsible for broadening the coherence peaks (Supplementary Material Note VII). Inter-band scattering, instead couples the energies of the gaps such that they approach each other. Note that similar spatial patterns for SFT#3 are shown in detail in the Supplementary

Material Note IX.

These results illustrate, how scattering in two band superconductors couples the two order parameters and demonstrates that this coupling can be locally resolved and even engineered. Both extremes, i.e. of mostly decoupled condensates with two independent gaps and fully coupled condensates with only a single gap, can be realized in near proximity to each other in the same material.

#### D. Discussion

Our results show that a topological defect in form of a stacking fault locally alters the superconducting properties in a multiband system via drastic changes in the intra- and inter-band coupling in agreement with the expectation of a model put forward by Sung and Wong [7], where both inter- and intra-band scattering processes are included. The intra-band coupling is mostly responsible for lifetime broadening of the individual coherence peaks, while the inter-band coupling changes their relative energies. Eventually, strong inter-band coupling merges the gap magnitudes to a common value, making the density of states indistinguishable from the one of a single band system. Intra- and inter-band scattering events can be understood on basis of the two Fermi surfaces. At a stacking fault, electrons of each band will be partially reflected staying on the same band, as the electronic dispersion relation at both sides of the stacking fault differs due to the Fm-3m symmetry of fcc, i.e. the Fermi surface only shows a threefold rotational symmetry and a stacking fault (stacking ABCABC|BCABC, where the missing 'A' layer creates the fault) represents a shift by about one-third of the full lattice translation along the close-packed (111) plane. Moreover, the stacking fault also induces scattering between the two Fermi surfaces, as the momentum of the electron perpendicular to the stacking fault is not conserved. Fits of the spectra to the Sung and Wong model show a strong enhancement of the inter-band scattering  $\Gamma_{12}$  and  $\Gamma_{21}$  on the whole top stacking fault of the SFT. This enhanced inter-band scattering extends out even beyond the SFT most likely due to electronic states with a finite momentum parallel to the surface. Note that the two scattering rates need to conserve the total number of electrons on each band, i.e. they are proportional to the DOS of each band (see Methods) and Fig. 4 (c) and (d) show the same pattern. Intra-band scattering, however, may independently vary on each band as the reflection probability of Bloch states on the two bands by a stacking fault

depends on the dispersion of the respective band. This is also reflected by the difference in the pattern of Figs. 4 (a) and (b). Due to the more symmetric shape of the compact Fermi surface, reflection at stacking faults is less expressed in comparison to the more asymmetric structure of the open Fermi surface. This is reflected in the generally higher values for intra-band scattering  $\Gamma_1$  in the triangle region.

The engineering of inter-band coupling is also of more fundamental interest. The pristine Pb crystal possesses two nearly decoupled condensates that can be coupled through inter-band scattering at defects. Especially, if the superconducting phase of the two bands laterally differ, e.g. by introducing a magnetic field, this engineering can lead to frustration of excitations such as vortices of solitonic modes. The control over the inter-band coupling in a two-band superconductor may allow to test for several predicted quantum effects, such as solitons [27, 28], vortices with fractional flux [29], non-Abrikosov vortices [30], topological knots [30], or the Leggett mode [31]. For example, the Leggett mode or soliton energy is a function of inter-band coupling and a shift of these mode as function of distance from a SFT would verify the nature of the modes.

### III. METHODS

*a. Experimental details:* All experiments were performed using a home-built scanning tunneling microscope with dilution refrigeration at below 45 mK [61]. The bias voltage  $U$  was applied between sample and common machine ground so that a positive bias voltage probes the unoccupied states of the sample. The STM chamber was kept at a base pressure of  $1 \times 10^{-10}$  mbar. The hat-shaped single crystal Pb(111) (miscut angle:  $\pm 0.1^\circ$ , purity: 99.999%) has been purchased from MaTecK GmbH. At a base pressure of  $1 \times 10^{-10}$  mbar the Pb crystal was prepared in cycles of hot sputtering with  $\text{Ar}^+$  ions of 3 keV at moderate temperatures ( $\sim 30 - 60^\circ\text{C}$ ) and subsequent annealing at  $190^\circ\text{C}$ . Following that, it was pre-cooled on a 78 K stage and then directly transferred into the STM in-situ, where it was cooled down to the base temperature in zero field. A tungsten tip was prepared by high-temperature flashing and soft dipping into a Au(111) surface. The differential conductance was measured using a Lock-in amplifier at a frequency of 3.0 – 3.8 kHz.

*b. Sung-Wong model:* To extract inter- and intra-band scattering induced by SFTs, the S&W model [7] was used to fit tunneling spectroscopy of superconducting gaps. First,

the tunneling spectroscopy is the sum of two BCS form tunneling DOS with temperature broadening.

$$\frac{dI}{dU}(eU) = \sum_{i=1,2} \sigma_i \operatorname{Re}\left(\frac{|u_i|}{\sqrt{u_i^2 - 1}}\right) * f'. \quad (1)$$

$\sigma_i$  denotes the band-specific differential conductance with  $\sigma_i = W_i N_i(E_F)$  [15, 69, 71]. Hereinafter  $i = 1, 2$  denotes the band index.  $W_i$  is the momentum averaged tunneling probability.  $N_i(E_F)$  is the DOS at Fermi energy.  $\operatorname{Re}$  is the real part of the function.  $f'$  is the derivative of the Fermi-Dirac distribution with respect to energy at temperature  $T$ .  $*$  is the convolution due to the temperature-induced broadening.

Second,  $u_i$  are determined by the coupled equations that are self-consistent [7, 8, 65],

$$u_1 \Delta_1^0 = |E| + i\Gamma_1 + i\Gamma_{12} \frac{u_2 - u_1}{\sqrt{u_2^2 - 1}}, \quad (2)$$

$$u_2 \Delta_2^0 = |E| + i\Gamma_2 + i\Gamma_{21} \frac{u_1 - u_2}{\sqrt{u_1^2 - 1}}. \quad (3)$$

$\Gamma_\lambda$  is the intra-band coupling, and  $\Gamma_{ij}$  is the inter-band coupling with scattering from band  $i$  to  $j$ . In addition,  $\Gamma_{12}$  and  $\Gamma_{21}$  are related by the equilibrium condition.

$$\frac{\Gamma_{12}}{\Gamma_{21}} = \frac{N_2(E_F)}{N_1(E_F)}. \quad (4)$$

$\Delta_\lambda^0$  is the intrinsic order parameter, which is caused by the phonon-mediated attractive interaction [73]. We argue that there is only intra-band pairing in Pb, as inter-band pairing results in pair density wave, which is not observed in our measurements. In the defect-free area, the scatterings are very small. The ratio  $\eta = \frac{N_{02}(E_F)}{N_{01}(E_F)} = 0.46$  can be obtained from the first-principles calculations with  $N_{02}(E_F) = 0.162$  (1/eV) for the compact Fermi surface and  $N_{01}(E_F) = 0.335$  (1/eV) for the open Fermi surface. By this we obtained the tunneling probability  $W_i$  for each band in our measurements. These tunneling probabilities are then used in the S&W model fitting for SFTs. We fitted the defect-free spectroscopy and obtained  $\Delta_i^0$ . We treat  $\Delta_i^0$  as constant when fitting data in the vicinity of SFTs. Then, the gap changes are induced by superconducting proximity due to SFT scatterings. We point out that Pb is a conventional two-band superconductor with same sign (same phase)

of the gap on the different Fermi surface sheets. As a result of impurity scattering, the gaps become energy-dependent and complex in Eqs. 2 and 3. We note that the intra- and inter-band couplings are homogeneous where there are no defects or impurities. However, the intra- and inter-band scatterings are spatially dependent around defects or impurities.

*c. First-principles calculations:* Density functional calculations of the electronic structure of Pb were carried out in the framework of the mixed-basis pseudopotential method [74, 75]. The electron-ion interaction was represented by norm-conserving relativistic pseudopotentials [76]. Spin-orbit coupling was incorporated within the pseudopotential scheme via Kleinman's formulation [77] and was consistently taken into account in the charge self-consistency cycle using a spinor representation of the wave functions. Further details of the spin-orbit coupling implementation within the mixed-basis pseudopotential method can be found in a previous publication [78]. For higher accuracy,  $5d$  semicore states were included in the valence space. The deep  $d$  potential is efficiently treated by the mixed-basis approach, where valence states are expanded in a combination of plane waves and local functions. Here, local functions of  $d$  type at the Pb sites were combined with plane waves up to a kinetic energy of 20 Ry. Brillouin-zone integration was performed by sampling a  $32 \times 32 \times 32$   $k$ -point mesh (corresponding to 2992  $k$  points in the irreducible part of the Brillouin zone) in conjunction with a Gaussian broadening of 0.2 eV. The exchange-correlation functional was represented by the local-density approximation in the parameterization of Perdew-Wang [79].

#### IV. DATA AVAILABILITY

All data needed to evaluate the conclusions in the paper are presented in the paper and the Supplemental Materials.

#### V. REFERENCES

- 
- [1] J. Bardeen, L. N. Cooper, and J. R. Schrieffer, Phys. Rev. **106**, 162 (1957).
  - [2] R. C. Dynes, V. Narayanamurti, and J. P. Garno, Phys. Rev. Lett. **41**, 1509 (1978).

- [3] F. Herman and R. Hlubina, *Phys. Rev. B* **94**, 144508 (2016).
- [4] H. Suhl, B. T. Matthias, and L. R. Walker, *Phys. Rev. Lett.* **3**, 552 (1959).
- [5] W. L. McMillan, *Phys. Rev.* **175**, 537 (1968).
- [6] C. Noce and L. Maritato, *Phys. Rev. B* **40**, 734 (1989).
- [7] C. C. Sung and V. K. Wong, *J. Phys. Chem. Solids* **28**, 1933 (1967).
- [8] N. Schopohl and K. Scharnberg, *Solid State Commun.* **22**, 371 (1977).
- [9] I. M. Tang, *Phys. Rev. B* **2**, 129 (1970).
- [10] W. S. Chow, *Phys. Rev. B* **4**, 111 (1971).
- [11] P. W. Anderson, *J. Phys. Chem. Solids* **11**, 26 (1959).
- [12] M. Hoyer, M. S. Scheurer, S. V. Syzranov, and J. Schmalian, *Phys. Rev. B* **91**, 054501 (2015).
- [13] G. Binnig, A. Baratoff, H. E. Hoenig, and J. G. Bednorz, *Phys. Rev. Lett.* **45**, 1352 (1980).
- [14] J. Nagamatsu, N. Nakagawa, T. Muranaka, Y. Zenitani, and J. Akimitsu, *Nature* **410**, 63 (2001).
- [15] Y. Noat, T. Cren, F. Debontridder, D. Roditchev, W. Sacks, P. Toulemonde, and A. San Miguel, *Phys. Rev. B* **82**, 014531 (2010).
- [16] M. Zehetmayer and H. W. Weber, *Phys. Rev. B* **82**, 014524 (2010).
- [17] M. Ruby, B. W. Heinrich, J. I. Pascual, and K. J. Franke, *Phys. Rev. Lett.* **114**, 157001 (2015).
- [18] Z. Du, X. Yang, H. Lin, D. Fang, G. Du, J. Xing, H. Yang, X. Zhu, and H. H. Wen, *Nat. Commun.* **7**, 10565 (2016).
- [19] A. Floris, A. Sanna, S. Massidda, and E. K. U. Gross, *Phys. Rev. B* **75**, 054508 (2007).
- [20] T. G. Saunderson, J. F. Annett, B. Újfalussy, G. Csire, and M. Gradhand, *Phys. Rev. B* **101**, 064510 (2020).
- [21] T. Gozlinski, Q. Li, R. Heid, R. Nemoto, R. Willa, T. K. Yamada, J. Schmalian, and W. Wulfhekel, *Sci. Adv.* **9**, eadh9163 (2023).
- [22] T.-S. Choy, J. Naset, J. Chen, S. Hershfield, and C. Stanton, *Bull. Am. Phys. Soc.* **45**, L36 (2000).
- [23] D. C. Mattis and J. Bardeen, *Phys. Rev.* **111**, 412 (1958).
- [24] A. A. Abrikosov and L. P. Gor'kov, *Sov. Phys. JETP* **35**, 1090 (1959).
- [25] J. Bardeen, *Rev. Mod. Phys.* **34**, 667 (1962).
- [26] K. Maki, *Prog. Theor. Phys.* **29**, 333 (1963).
- [27] Y. Tanaka, *Phys. Rev. Lett.* **88**, 017002 (2002).

- [28] S. V. Kuplevakhsky, A. N. Omelyanchouk, and Y. S. Yerin, *Low Temp. Phys.* **37**, 667 (2011).
- [29] E. Babaev, *Phys. Rev. Lett.* **89**, 067001 (2002).
- [30] Y. M. Cho and P. Zhang, *Phys. Rev. B* **73**, 180506 (2006).
- [31] A. J. Leggett, *Prog. Theor. Phys.* **36**, 901 (1966).
- [32] A fourth type of defect are the small protrusions scattered throughout the image. These, however, are not intrinsic to the material or the preparation but caused by the interaction between surface and tip: In this case, an earlier (large) scale image was recorded, where the tip speed and feedback conditions were chosen in a way to minimize the time needed to find these SFTs, at the cost of occasional, unwanted tip-sample interactions at step edges, where single lead atoms would be pulled out and dragged along the line of scan before being dropped again.
- [33] M. Müller, N. Néel, S. Crampin, and J. Kröger, *Phys. Rev. Lett.* **117**, 136803 (2016).
- [34] M. Müller, N. Néel, S. Crampin, and J. Kröger, *Phys. Rev. B* **96**, 205426 (2017).
- [35] S. Y. Song and J. Seo, *Sci. Rep.* **7**, 12177 (2017).
- [36] J. F. Wolf and H. Ibach, *Appl. Phys. A* **52**, 218 (1991).
- [37] J. Engbæk, J. Schiøtz, B. Dahl-Madsen, and S. Horch, *Phys. Rev. B* **74**, 195434 (2006).
- [38] A. Y. Aladyshkin, A. S. Aladyshkina, and S. I. Bozhko, *J. Phys. Chem. C* **125**, 26814 (2021).
- [39] J. Silcox and P. B. Hirsch, *Philos. Mag.* **4**, 72 (1959).
- [40] R. M. J. Cotterill, *Philos. Mag.* **6**, 1351 (1961).
- [41] M. J. Yokota and J. Washburn, *Philos. Mag.* **16**, 459 (1967).
- [42] F. Bonsignori, V. Bortolani, and G. Velo, *Nuovo Cimento B* **57**, 194 (1968).
- [43] Q. F. Guan, L. Pan, H. Zou, A. M. Wu, S. Z. Hao, Q. Y. Zhang, C. Dong, and G. T. Zou, *J. Mater. Sci.* **39**, 6349 (2004).
- [44] R. Schäublin, Z. Yao, N. Baluc, and M. Victoria, *Philos. Mag.* **85**, 769 (2005).
- [45] G. J. Hardy and M. L. Jenkins, *Philos. Mag.* **52**, L19 (2006).
- [46] Y. Matsukawa, Y. N. Osetsky, R. E. Stoller, and S. J. Zinkle, *Philos. Mag.* **88**, 581 (2008).
- [47] K. Schouteden and C. Van Haesendonck, *Phys. Rev. Lett.* **108**, 076806 (2012).
- [48] J. Wei Wang, S. Narayanan, J. Yu Huang, Z. Zhang, T. Zhu, and S. X. Mao, *Nat. Commun.* **4**, 2340 (2013).
- [49] K. Y. Yu, D. Bufford, C. Sun, Y. Liu, H. Wang, M. A. Kirk, M. Li, and X. Zhang, *Nat. Commun.* **4**, 1377 (2013).

- [50] K. Schouteden, B. Amin-Ahmadi, Z. Li, D. Muzychenko, D. Schryvers, and C. Van Haesendonck, *Nat. Commun.* **7**, 14001 (2016).
- [51] B. P. Uberuaga, R. G. Hoagland, A. F. Voter, and S. M. Valone, *Phys. Rev. Lett.* **99**, 135501 (2007).
- [52] X. Zhang, K. Hattar, Y. Chen, L. Shao, J. Li, C. Sun, K. Yu, N. Li, M. L. Taheri, H. Wang, J. Wang, and M. Nastasi, *Prog. Mater. Sci.* **96**, 217 (2018).
- [53] M. Ohmori, H. Hirayama, and K. Takayanagi, *Phys. Rev. B* **59**, 5612 (1999).
- [54] Y. N. Osetsky, D. Rodney, and D. J. Bacon, *Philos. Mag.* **86**, 2295 (2006).
- [55] Y. Guo, Y.-F. Zhang, X.-Y. Bao, T.-Z. Han, Z. Tang, L.-X. Zhang, W.-G. Zhu, E. G. Wang, Q. Niu, Z. Q. Qiu, J.-F. Jia, Z.-X. Zhao, and Q.-K. Xue, *Science* **306**, 1915 (2004).
- [56] M. Schackert, T. Märkl, J. Jandke, M. Hölzer, S. Ostanin, E. K. U. Gross, A. Ernst, and W. Wulfhekel, *Phys. Rev. Lett.* **114**, 047002 (2015).
- [57] O. Kurnosikov, O. A. O. Adam, H. J. M. Swagten, W. J. M. de Jonge, and B. Koopmans, *Phys. Rev. B* **77**, 125429 (2008).
- [58] O. Kurnosikov, J. H. Nietsch, M. Sicot, H. J. M. Swagten, and B. Koopmans, *Phys. Rev. Lett.* **102**, 066101 (2009).
- [59] O. Kurnosikov, H. J. M. Swagten, and B. Koopmans, *Phys. Rev. Lett.* **106**, 196803 (2011).
- [60] A. Weismann, M. Wenderoth, S. Lounis, P. Zahn, N. Quaas, R. G. Ulbrich, P. H. Dederichs, and S. Blügel, *Science* **323**, 1190 (2009).
- [61] T. Balashov, M. Meyer, and W. Wulfhekel, *Rev. Sci. Instrum.* **89**, 113707 (2018).
- [62] M. Uhl, P. Kot, R. Drost, H. Huang, J. Ankerhold, J. C. Cuevas, and C. R. Ast, *Phys. Rev. Res.* **6**, 043233 (2024).
- [63] J. Tersoff and D. R. Hamann, *Phys. Rev. B* **31**, 805 (1985).
- [64] H. Schmidt, J. F. Zasadzinski, K. E. Gray, and D. G. Hinks, *Phys. Rev. Lett.* **88**, 127002 (2002).
- [65] M. Iavarone, G. Karapetrov, A. E. Koshelev, W. K. Kwok, G. W. Crabtree, D. G. Hinks, W. N. Kang, E.-M. Choi, H. J. Kim, H.-J. Kim, and S. I. Lee, *Phys. Rev. Lett.* **89**, 187002 (2002).
- [66] T. Ekino, T. Takasaki, T. Muranaka, J. Akimitsu, and H. Fujii, *Phys. Rev. B* **67**, 094504 (2003).
- [67] H. Schmidt, J. F. Zasadzinski, K. E. Gray, and D. G. Hinks, *Physica C* **385**, 221 (2003).

- [68] J. A. Silva-Guillén, Y. Noat, T. Cren, W. Sacks, E. Canadell, and P. Ordejón, *Phys. Rev. B* **92**, 064514 (2015).
- [69] Y. Noat, J. A. Silva-Guillén, T. Cren, V. Cherkez, C. Brun, S. Pons, F. Debontridder, D. Roditchev, W. Sacks, L. Cario, P. Ordejón, A. García, and E. Canadell, *Phys. Rev. B* **92**, 134510 (2015).
- [70] J. Senkpiel, C. Rubio-Verdú, M. Etzkorn, R. Drost, L. M. Schoop, S. Dambach, C. Padurariu, B. Kubala, J. Ankerhold, C. R. Ast, and K. Kern, *Phys. Rev. B* **100**, 014502 (2019).
- [71] Y. Noat, T. Cren, P. Toulemonde, A. San Miguel, F. Debontridder, V. Dubost, and D. Roditchev, *Phys. Rev. B* **81**, 104522 (2010).
- [72] S. Datta, A. Vasdev, S. Halder, J. Singh, Y. Singh, and G. Sheet, *J. Phys.: Condens. Matter* **32**, 315701 (2020).
- [73] A. E. Karakozov, E. G. Maksimov, and Y. G. Ponomarev, *JETP Lett.* **91**, 24 (2010).
- [74] C. Elsasser, N. Takeuchi, K. M. Ho, C. T. Chan, P. Braun, and M. Fahnle, *J. Phys.: Condens. Matter* **2**, 4371 (1990).
- [75] B. Meyer and M. Fahnle, *Phys. Rev. B* **56**, 13595 (1997).
- [76] D. Vanderbilt, *Phys. Rev. B* **32**, 8412 (1985).
- [77] L. Kleinman, *Phys. Rev. B* **21**, 2630 (1980).
- [78] R. Heid, K. P. Bohnen, I. Y. Sklyadneva, and E. V. Chulkov, *Phys. Rev. B* **81**, 174527 (2010).
- [79] J. P. Perdew and Y. Wang, *Phys. Rev. B* **45**, 13244 (1992).

## VI. ACKNOWLEDGEMENTS

We are grateful for discussions with Roland Willa, Horst Hahn, Marcel Rost and Reinhard Schneider.

## VII. AUTHOR CONTRIBUTIONS

Experiments have been carried out by T.G., Q.L., A.H., R.N. and supervised by W.W.. The experimental data has been evaluated by T.G., Q.L. and O.K.. DFT calculations have been performed by R.H.. Theory was performed by Q.L., T.G., J.S. and W.W.. The manuscript was written by Q.L., T.G. and W.W. with input from all authors. Samples were supplied by R.N. and T.K.Y.

## **VIII. FUNDING**

The authors acknowledge funding by the Deutsche Forschungsgemeinschaft (DFG) under the grant CRC TRR 288 - 422213477 “ElastoQMat,” projects B06 and B01 and support by JSPS KAKENHI under the grant number 17K19023.

## **IX. COMPETING INTERESTS**

The authors declare that they have no competing interests.

## **X. ADDITIONAL INFORMATION**

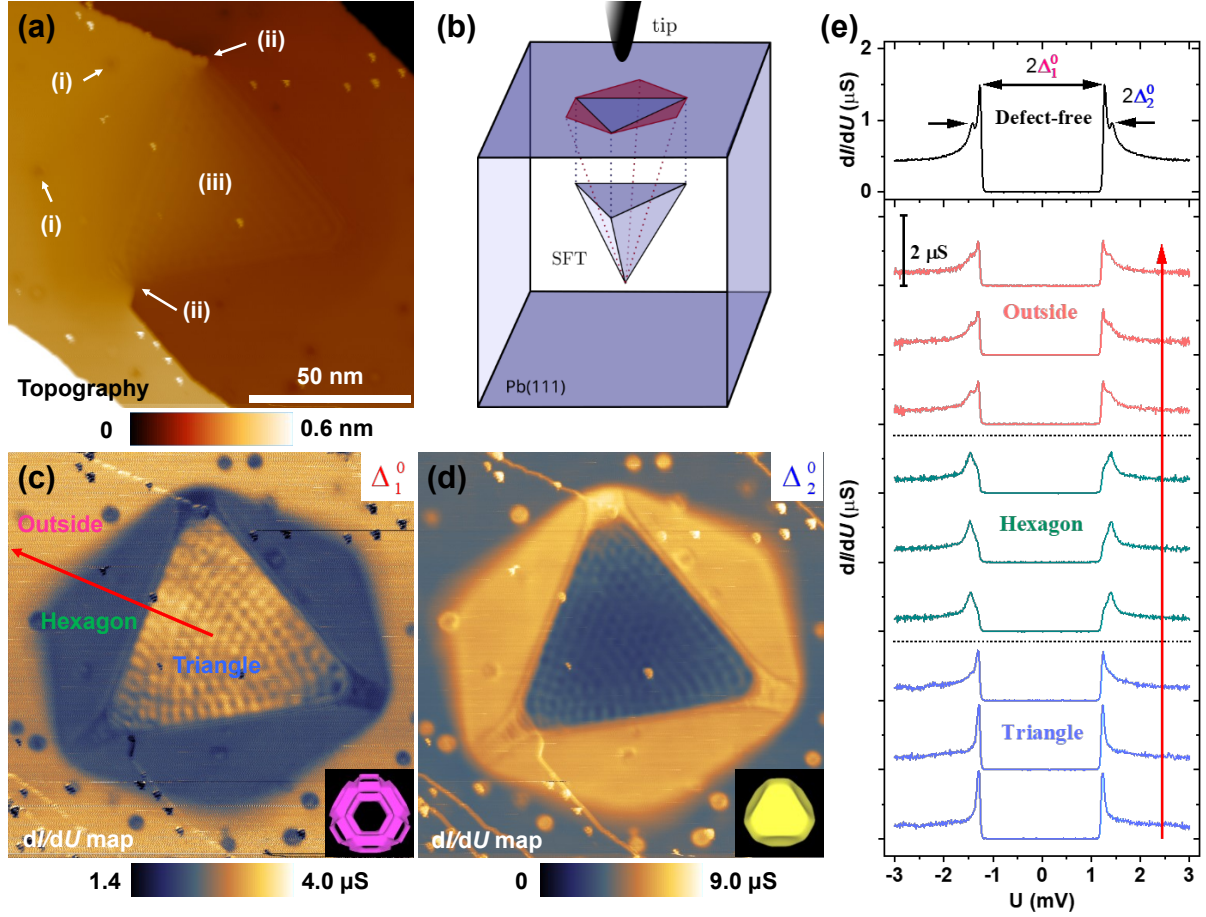
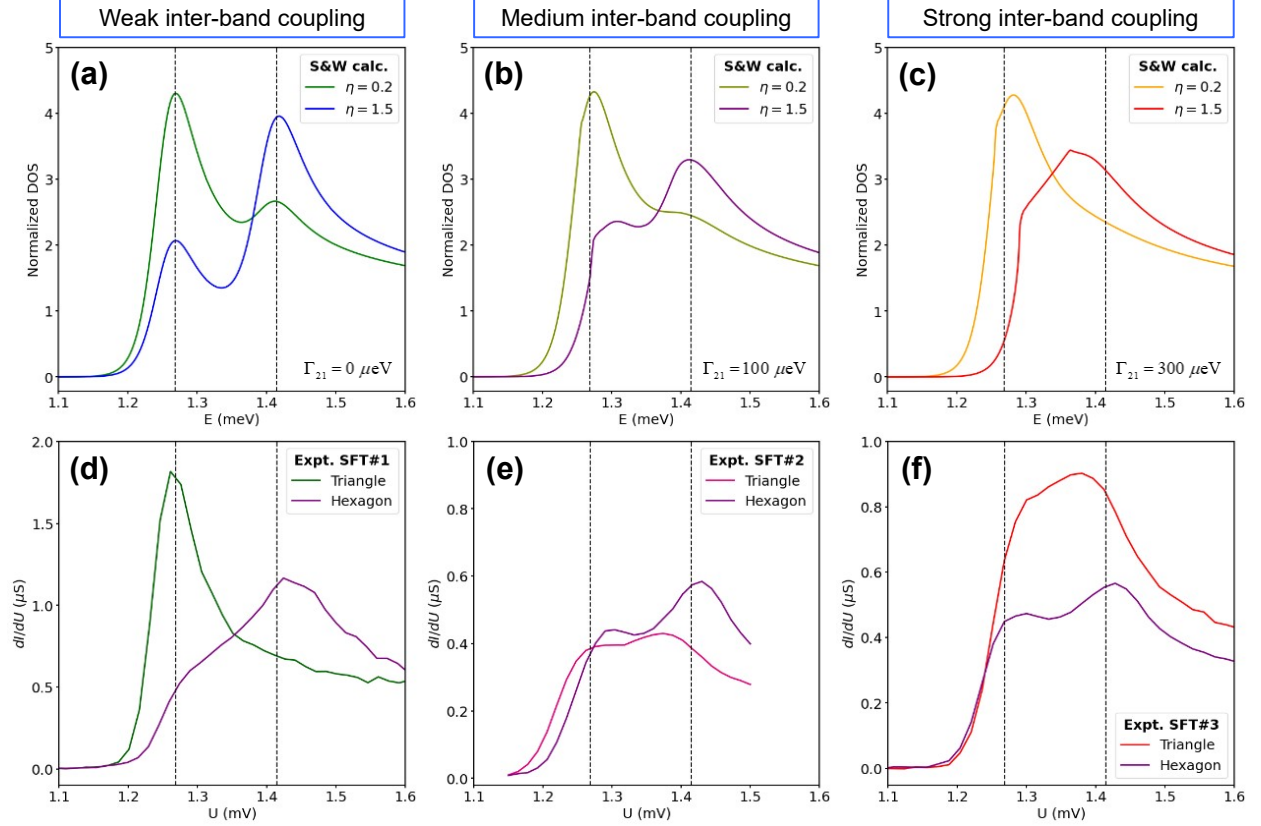


FIG. 1. Influence of stacking fault tetrahedron on superconducting gaps (SFT#1). (a) Topography measured with sample bias  $U = 1.4$  mV and tunneling current  $I = 1$  nA. Three types of defects are indicated as (i) argon bubbles or small vacancy conglomerates, (ii) a screw dislocation and (iii) a buried stacking fault tetrahedron. (b) Sketch of the STM measuring a subsurface stacking fault tetrahedron in Pb(111). (c)  $dI/dU$  mapping at  $\Delta_1^0$ . The inset shows the corresponding open Fermi surface [22]. (d)  $dI/dU$  mapping at  $\Delta_2^0$ . The inset shows the corresponding compact Fermi surface [22]. The  $dI/dU$  maps in (c) and (d) were measured with tip stabilized at  $U = 1.4$  mV and  $I = 1$  nA and lock-in modulation amplitude of  $U_{mod} = 50$   $\mu$ V and frequency of 3.751 kHz. (e)  $dI/dU$  spectra on defect-free area (top panel) and at different regions from triangle center to outside the SFT along the red arrow in panel (c). For  $dI/dU$  spectra measurements across the SFT, the tip was stabilized at  $U = 3$  mV and  $I = 1$  nA, with lock-in modulation  $U_{mod} = 20$   $\mu$ V for the amplitude and frequency of 3.751 kHz. For  $dI/dU$  spectra on defect-free area, the tip was stabilized at the same tunneling condition with lock-in modulation amplitude of  $U_{mod} = 20$   $\mu$ V and frequency of 3.041 kHz.



**FIG. 2. Influence of inter-band coupling on two-band superconducting gaps.** (a)-(c) Demonstration of inter-band coupling on two-band superconducting gaps with different DOS ratio  $\eta$  ( $= N_2(E_F)/N_1(E_F) = \Gamma_{12}/\Gamma_{21}$ ) from weak to strong inter-band coupling. (a) No inter-band coupling. The intensity of coherence peaks depends on the DOS ratio of two bands, but without energy variation of coherence peaks. (b) Medium inter-band coupling. (c) Strong inter-band coupling. Only one coherence peak can be seen for the strong inter-band coupling. The green to orange color corresponds to increasing inter-band coupling for low DOS ratio. The blue to red color corresponds to increasing inter-band coupling for high DOS ratio. (d)-(f) Spectra at triangle and hexagonal regions for different SFTs. (d) Spectra for SFT#1 (see also Fig. 1(e)). (e) Spectra for SFT#2. (f) Spectra for SFT#3. Hexagonal regions always have a medium inter-band coupling with high DOS ratio, while the inter-band coupling and DOS ratio at triangular regions vary from weak to strong. The dashed lines marked the coherence peaks for defect-free spectroscopy in Fig. 1(e). In panels (e) and (f), the tip was stabilized at  $U = 100$  mV and  $I = 1$  nA, with tip height  $z$  offset -120 pm for the  $dI/dU$  spectroscopy. The lock-in amplifier has a modulation with amplitude of  $U_{mod} = 20$   $\mu$ V and frequency of 3.402 kHz.

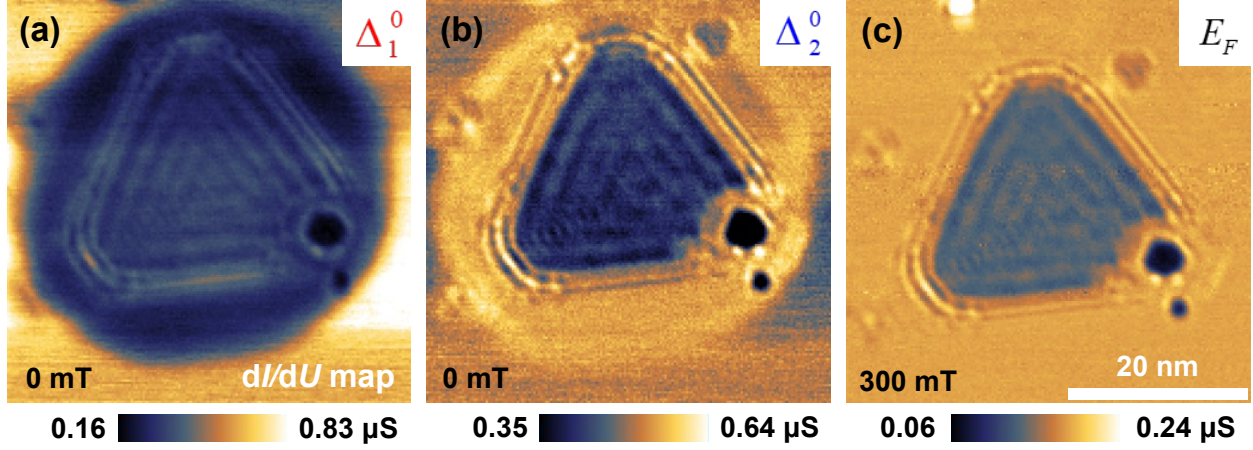


FIG. 3. **Small SFT without screw dislocations (SFT#2).** (a)  $dI/dU$  map at  $\Delta_1^0$ . (b)  $dI/dU$  map at  $\Delta_2^0$ . (c)  $dI/dU$  map for normal states at Fermi energy measured at 300 mT. The tip was stabilized at  $U = 100$  mV and  $I = 1$  nA, with tip height  $z$  offset -120 pm for the  $dI/dU$  spectroscopy. The lock-in amplifier has a modulation with amplitude of  $U_{mod} = 20$   $\mu\text{V}$  and frequency of 3.402 kHz.

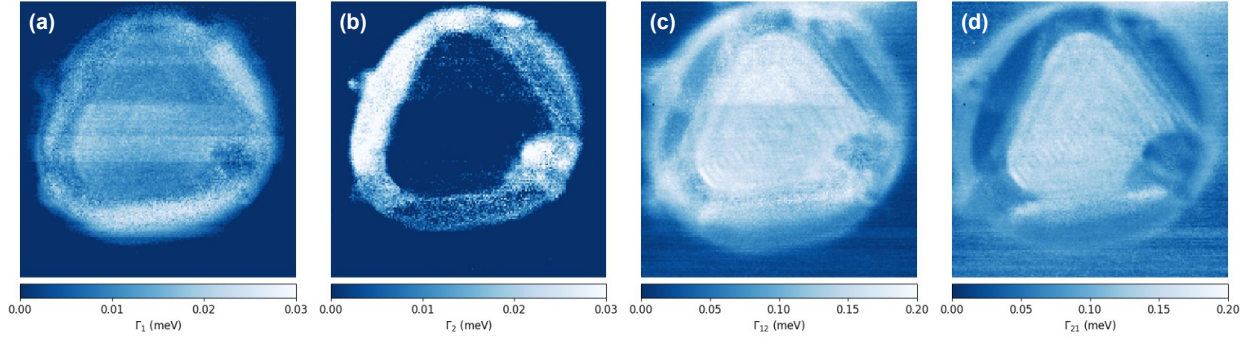


FIG. 4. **Spatially resolved intra- and inter-band couplings (SFT#2).** (a) Spatially resolved intra-band coupling  $\Gamma_1$ . (b) Spatially resolved intra-band coupling  $\Gamma_2$ . (c) Spatially resolved inter-band coupling  $\Gamma_{12}$ . (d) Spatially resolved inter-band coupling  $\Gamma_{21}$ .